

Article

On the Estimation of the Wave Energy Period and a Kernel Proposal for the Peru Basin

Dennys De La Torre ^{1,*}, Jaime Luyo ¹ and Arturo Ortega ²

¹ Universidad Nacional de Ingeniería, Av. Túpac Amaru 210, Rímac, Lima 15333, Peru; jluyok@uni.edu.pe

² Universidad Autónoma del Perú, Panamericana Sur Km. 16.3, Villa El Salvador, Lima 15842, Peru; arturo.ortega@autonoma.pe

* Correspondence: ddelatorrec@uni.edu.pe

Abstract: The energy period is a crucial parameter needed for assessing wave energy. This parameter is regularly approximated using standard wave spectrums that do not always characterise an actual ocean region, even more if this region is far from the Northern Hemisphere, where most of the energy period approximations have been developed. In this work, diverse approximations for the energy period were evaluated using spectral data from a region of the Peru Basin. It included the assessment of a proposed Kernel “coefficient” curve. They were assessed regarding their time series, wave climate, and temporal variability. The time series analysis showed that the approximations based on the peak period do not have a realistic physical representation of ocean waves. On the other hand, the proposed Kernel correlation gave the best results for computing the energy period and the monthly/seasonal variability indexes for temporal variability analysis. Additionally, the correlations based on the zero-up-crossing period generated the best results for computing the coefficient of variation. Conversely, the highest errors were calculated for the correlations based on the traditional Bretschneider and JONSWAP spectrums. The wave climate indicated an annual average energy period equal to 9.8 s, considered stable due to its low variability.

Keywords: wave energy period; wave climate; spectral data; Kernel regression; Bretschneider spectrum; JONSWAP spectrum; Peru Basin



Citation: De La Torre, D.; Luyo, J.; Ortega, A. On the Estimation of the Wave Energy Period and a Kernel Proposal for the Peru Basin. *J. Mar. Sci. Eng.* **2023**, *11*, 1100. <https://doi.org/10.3390/jmse11061100>

Academic Editors: Almudena Filgueira-Vizoso, Laura Castro-Santos and Diego Vicinanza

Received: 4 April 2023
Revised: 4 May 2023
Accepted: 16 May 2023
Published: 23 May 2023



Copyright: © 2023 by the authors. Licensee MDPI, Basel, Switzerland. This article is an open access article distributed under the terms and conditions of the Creative Commons Attribution (CC BY) license (<https://creativecommons.org/licenses/by/4.0/>).

1. Introduction

In the race to generate environmentally friendly electricity, the power from ocean waves is one of the most promising. Prior to the deployment of a wave energy farm, an accurate assessment of the wave energy resource has to be carried out. Wave power can be calculated based on diverse spectral parameters, such as the significant wave high and the energy period. Nevertheless, the last parameter, or failing that, the spectral wave density data, is only sometimes supplied by the buoy administrators. The state-of-the-art presents diverse approximations for the energy period, primarily based on the standard wave spectrums; however, they are not always representative of the actual ocean region of interest.

The Pierson–Moskowitz standard wave spectrum has often been used for fully developed sea states (open sea), while the JONSWAP spectrum has been used for partially developed sea states (fetch-limited sea) [1]. According to the open literature, several wave energy assessments have been carried out for open sea using the Pierson–Moskowitz or JONSWAP spectrum, for example, off the coast of Galicia [2], along the northwest coast of the Iberian Peninsula [3], off the coasts of the United States [4], and in the evaluation of the wave energy resources of the Peruvian sea [5].

A particular case is the assessment of offshore wave energy resources in the East China Sea [6]. That work assumed a JONSWAP spectrum following the presumption made by the wave energy resources assessment of off Canada’s coasts [7], the North Sea [8] and for the

global study of the oceans [9]. Another case is the wave energy resource assessment for the Hawaii multimodal sea state [10]. It was based on the Pierson–Moskowitz spectrum because the International Electrotechnical Commission Technical Committee-114 (IEC TC-114) suggests using that spectrum to calculate wave energy when the energy period is not available. In contrast, the wave spectrum designed by the Atlantic Marine Energy Test Site (AMETS), Ireland, was found to fit relatively well for open water sites, as shown by the similarity of its spectral shape when compared with the Bretschneider spectrum [11].

According to the previous works, when there is no available spectral data, a predefined standard spectral form is selected; in most cases, the JONSWAP spectrum has been used. However, this assumption may considerably overestimate the wave energy during its assessment, as demonstrated by [12]. In that work, using a Bretschneider spectrum, the wave power of the Peru Basin was estimated to be almost 22 kW/m, in contrast to the 32 kW/m reported by [5], who used a JONSWAP spectrum. Even more, using standard spectrums primarily developed for the Northern Hemisphere does not guarantee an accurate assessment of the wave power, as shown by [13], who used spectral data of the Peru Basin for calculating wave power and found errors of up to 16% compared to the values calculated using standard spectrums.

To manage that issue, efforts have been made to mathematically model wave periods and spectrums. Ref. [14] presented an empirical altimeter wave period model based on the relationship between the wave period with the radar backscatter coefficient from satellite altimeter data and the significant wave height from buoy measurements. Later, ref. [15] developed a physical model for wave periods from altimeter data based on the weak turbulence theory of wind-driven waves. Thus, a peak period expression was presented from a relationship of instant wave characters (significant wave height variance and peak frequency) with wave responses (wave generation and dissipation). Similarly, ref. [16] proposed a model for wind wave dissipation based on the well-known Phillips spectrum [17]. The model considered the dissipation associated with the wave breaking, introducing a dissipation function dependent on the spectral energy flux. The function, expressed in terms of the energy spectrum, can be used for wave prediction.

Recently, a method based on inverse processes for modelling time-average frequency-directional spectrums was presented by [18]. An approximated wave spectrum is calculated from the definition of the zeroth-order moment, and this moment is computed from the definition of the significant wave height. Similarly, ref. [19] estimated wind wave zero-up-crossing period and significant wave height by implementing a stochastic simulation model. Generated time series were used to calculate wave power, assuming a linear relationship between energy and zero-up-crossing periods.

Numerical simulation of wave spectrum evolution in space and time by the spectral wave action equation [20] can be another alternative to manage the shortage of spectral data. In this context, ref. [21] simulated the French Atlantic and Channel coast using a wave generation and dissipation, bottom friction, and coastal reflection version of WAVEWATCH III (WWIII) [22]. Similarly, ref. [23] recalibrated WWIII modules for parameterizations of wind input, wave breaking, and swell dissipation terms. Thus, the modelled wave spectrums were validated against the Lake Michigan and 1-year global hindcasts. The models performed well in predicting significant wave height, wave period and representing high-frequency wave spectrum. Recently, ref. [24] evaluated spectral data (spectral variance density and mean spectral direction) generated by SWAN [25] and WWIII and compared them against Eastern Black Sea buoy measurements. The accuracy of the models showed dependency on the wave frequency range. Moreover, the estimated seasonal/annual averaged directional spectrums by SWAN matched the measurements better than those estimated by WWII.

In the present work, an evaluation of the diverse approximations for calculating the energy period of the Peru Basin is carried out. It includes using spectral data, local calibration coefficients, standard wave spectrums, and a proposed Kernel calibration curve. Moreover, a wave climate analysis of the energy period based solely on spectral data is also

presented. The work also includes monthly and seasonal distributions of the energy period and its annual variability.

After Section 1, the introduction, this paper is divided as follows. Section 2 introduces the ocean data, used for the analysis and the modelling based on spectral data, and the tuning coefficients, used for estimating the energy period. This section also presents a Kernel regression as an alternative to improve the energy period estimation. Then, the calculation of the variability of the energy period is explained. In Section 3, an analysis of the energy, zero-up-crossing and peak periods and the temporal variability of the energy period is carried out and compared with those generated by the diverse approximations. Finally, the main findings and contributions of this work are summarised.

2. Materials and Methods

2.1. Spectral Data

The spectral data for this work were obtained from the National Data Buoy Center (NDBC) [26], according to the spectral wave density information offered by Buoy 32012 deployed in the Peru Basin (Figure 1). The geographical location of this buoy is shown in Table 1, together with the sea depth at that position. The spectral data are provided hourly, containing a total of 52,608 sea states, with more than 99.3% of the data available from 2012 to 2017. Wave roses of wave power and significant wave height and scatter diagrams of relative frequencies and wave energy distribution using Buoy 32012 are presented in [27], which assessed wave energy resources in the Peru Basin.



Figure 1. Location of Buoy 32012 in the Peru Basin. The figure is taken from NDBC [26].

Table 1. Ocean Buoy 32012 deployed in the Peru Basin, providing historical data.

Buoy	Latitude (° S)	Longitude (° W)	Sea Depth (m)
32012	19.425	85.078	4524

2.2. Wave Period Modelling Based on Spectral Moments

The wave energy period or average period of component waves, T_e (s), corresponds to the period of an equivalent single sinusoidal wave with the same energy as the sea state. According to the moments of the wave spectrum theory [28,29], T_e can be estimated by:

$$T_e = \frac{m_{-1}}{m_0} \tag{1}$$

where m_{-1} and m_0 are the spectral moments of order -1 and 0 , respectively. T_e is a crucial parameter needed for the calculation of wave power. However, the available historical standard meteorological data usually do not consider T_e . Generally, they are limited to providing the significant wave height, peak period T_p (s), and zero-up-crossing period T_z (s).

The peak or dominant period corresponds to the frequency, in the spectral frequency band, with the maximum spectral density of a particular sea state. The zero-up-crossing period represents the average period of waves when they cross the mean sea surface level. This period can be calculated as follows:

$$T_z = \sqrt{\frac{m_0}{m_2}} \tag{2}$$

where m_2 is the spectral moment of order 2.

The moment of order n of the variance spectrum (m_n) or spectral moment is calculated as:

$$m_n = \int_0^\infty f^n S_\zeta(f) df \tag{3}$$

where S_ζ is the omnidirectional wave spectrum or spectral variance density (m^2/Hz) as a function of the wave frequency f (Hz). Wave spectral data consist of a finite number of components (k) of computed spectral energy density ($S_i = S_\zeta(f_i), i \in [1, k]$). Thus, for the sequential orders, the discrete form of the spectral moments is:

$$m_n = \sum_{i=1}^{k-1} 0.5(S_i f_i^n + S_{i+1} f_{i+1}^n)(f_{i+1} - f_i) \tag{4}$$

2.3. The Diverse Approximations for the Wave Energy Period

A series of coefficients correlating T_e with T_z and T_e with T_p can be calculated from the relation of the spectral moments defining T_e and T_z , Equations (1) and (2), respectively, and the relation of T_p with the wave spectrum. In general, this procedure results in the following linear relationship:

$$T_e = \lambda T_k \tag{5}$$

where λ is the calibration coefficient that defines the relation between T_e and T_k . The last can refer to T_p or T_z . λ depends on the wave spectrum and frequency.

In this context, an expected engineering practice is estimating T_e assuming standard wave spectrums and using available wave periods when the buoy administrators do not provide spectral data. Thus, when the sea has characteristic of fetch limited, a sea not completely developed, the JONSWAP standard spectrum can be assumed, and the relation between T_e and T_p is [29]:

$$T_e = 0.89 T_p \tag{6}$$

Now, if the sea is characterised as open, a sea wholly developed with a large fetch, the Bretschneider standard spectrum can be assumed, and the relation between T_e and T_p is [30]:

$$T_e = 0.857 T_p \tag{7}$$

According to [9,31], the relation between T_e and T_p goes from 0.86, broadband spectrums, to unity, narrowband spectrums, due to wave spectrum deformation in coastal seas. In this respect, ref. [32] considered λ equal to 1 for their preliminary assessment of wave energy resources in southern New England, similarly to [33] for analysing sea winds and land breeze effects on wave-wind energy in the nearshore of Tyrrhenian Sea.

Estimating T_e from T_p using Equation (5) has been common practice in wave energy engineering. However, that can increase uncertainties for the cases of combined sea states: long-crested swell and short-crested wind waves with two energy peaks in the spectrum at low and high frequencies, respectively, a situation that a standard spectrum with a solitary

peak period cannot capture. Several adjusted values for λ have been proposed to manage this situation, as described in [34].

Thus, for seas with large fetch (open sea) composed of waves generated by wind and swell waves, such as the Peru Basin, T_z is recommended to approach T_e , as the former represents an actual physical mean wave period. For this situation, based on the Bretschneider standard spectrum, a relation between T_e and T_z can be written as [30]:

$$T_e = 1.2T_z \tag{8}$$

For calculating the UK continental shelf wave power, ref. [35] stated a λ equal to 1.14 for wind wave and swell, assuming a representative JONSWAP spectrum. This assumption was followed in assessing the wave energy resources of the Santa Catarina coastline, south of Brazil [36], as they considered it a more conservative approach. In turn, ref. [37] followed the previous work for a wave energy resource study of the Maldives islands, with even the original assumption of the JONSWAP spectrum characteristic of the UK territorial waters.

In contrast to analytical procedures and making the most of the spectral data available in the Peru Basin, ref. [13] calculated local calibrations coefficients using linear regression and adjusted them for high-energy sea states. These “new” calibration coefficients (NCC), as [13] called them, are used to approach T_e as follows:

$$T_e = 0.8T_p \tag{9}$$

$$T_e = 1.25T_z \tag{10}$$

That work reported errors lower than 5% when validated utilising wave power calculated also using spectral data.

2.4. The Kernel Regression

The Kernel regression is a non-parametric localised regression method driven directly by data [38]. The idea is to predict the output at a specific point based on the observed data (inputs and outputs) near that specific point. The selection and influence of the data close to the specific point are achieved by the use of a Kernel function Γ , calculated utilising a Gaussian distribution:

$$\Gamma(x) = \frac{1}{h\sqrt{2\pi}} e^{-0.5\left(\frac{x-x_i}{h}\right)^2} \tag{11}$$

where x_i is the vector of the k input data for training, $i \in [1, k]$. x is each linearly spaced input value where the regression is calculated, and h is the Kernel bandwidth.

The estimated output value is computed by the weighted average of all input data points x_i selected by the Kernel function. Thus, for each of k input datum, its respective weight $W \in [0, 1]$ is calculated as:

$$W_i = \frac{\Gamma}{\sum_{i=1}^k \Gamma_i} \tag{12}$$

Then, the weights are used to compute the estimated output value of the regression Y , i.e., for each x :

$$Y_i = \sum_{i=1}^k y_i W_i \tag{13}$$

where y_i is the output and also training data corresponding to each x_i .

2.5. Temporal and Monthly/Seasonal Variability

The coefficient of variation (CV) quantifies the amount of changeability of a particular variable for all time scales [9]. For this work, the variable under study was T_e ; thus, CV was calculated as follows:

$$CV = \frac{\sigma(T_e)}{\mu(T_e)} \tag{14}$$

This parameter is computed regarding the analysed variable's standard deviation σ and average value μ . In this work, T_e was considered stable for CV lower than 0.2.

In contrast to the "all-time scales" CV, it is also possible to analyse the variability for defined short-time scales. Hence, concepts of monthly and seasonal variability index (MV and SV, respectively) are defined as:

$$MV = \frac{T_{emmax} - T_{emmin}}{T_{eyear}} \quad (15)$$

$$SV = \frac{T_{esmax} - T_{esmin}}{T_{eyear}} \quad (16)$$

where T_{emmax} and T_{emmin} represent the average T_e of the highest and lowest energetic month (m). This index represents the non-dimensional maximum monthly variation in T_e . A similar criterion is applied to SV (s season), and finally, T_{eyear} is the annual average value of T_e .

3. Results and Discussion

This section starts by analysing the energy, zero-up-crossing and peak periods. Then, a discussion about the diverse approximations for T_e is performed, and an alternative using a Kernel regression is proposed. After that, the temporal variability of T_e is analysed, and average values of T_e and CV for monthly and annual time scales are presented together with their estimated values using the diverse approximations. Concluding this section, the monthly and seasonal variability indexes and their estimated values using the diverse approximations are discussed. Over this section, a wave climate analysis regarding T_e is carried out.

3.1. Analysis of Time Series

The spectral data for computing the following time series came from Buoy 32012. They were selected from the beginning of 2012 to the end of 2017. This selection was due to the considerable data gaps outside the selected period. The calculated time series presented an unusual behaviour; the lowest values appeared during February 2014. It is hypothesised that this behaviour was due to the "El Niño" phenomenon [39] that happened that year.

Figure 2 presents the time series of the energy period calculated using the spectral moments according to Equation (1). The evolution of this period showed no notorious trend. Over time, T_e had unusual values higher than 18 s and lower than 5 s. Mainly, T_e varied from 7 s to 13 s.

A similar behaviour was presented for the zero-up-crossing period, Figure 3, again characterised by its unnoticeable trend over time. This period was also calculated based on the spectral data, with Equation (2). In contrast to the T_e time series, T_z presented shorter values, mostly from 5 s to 11 s.

The previous T_e and T_z time series presented a realistic behaviour characterised by the stochastic nature of the waves. On the other hand, Figure 4 shows the peak period time series obtained based on the spectral data but selected from the frequency corresponding to the highest value of the wave spectrum of a specific sea state, as explained above. Contrarily to the previous periods, T_p presented an unrealistic behaviour over the time domain. The curve profile presented a marked impact of the measurement frequency taken by the buoy. Even so, the range of this period was still trustable. However, its suitability oriented to the approximation of T_e needed to be more credible.

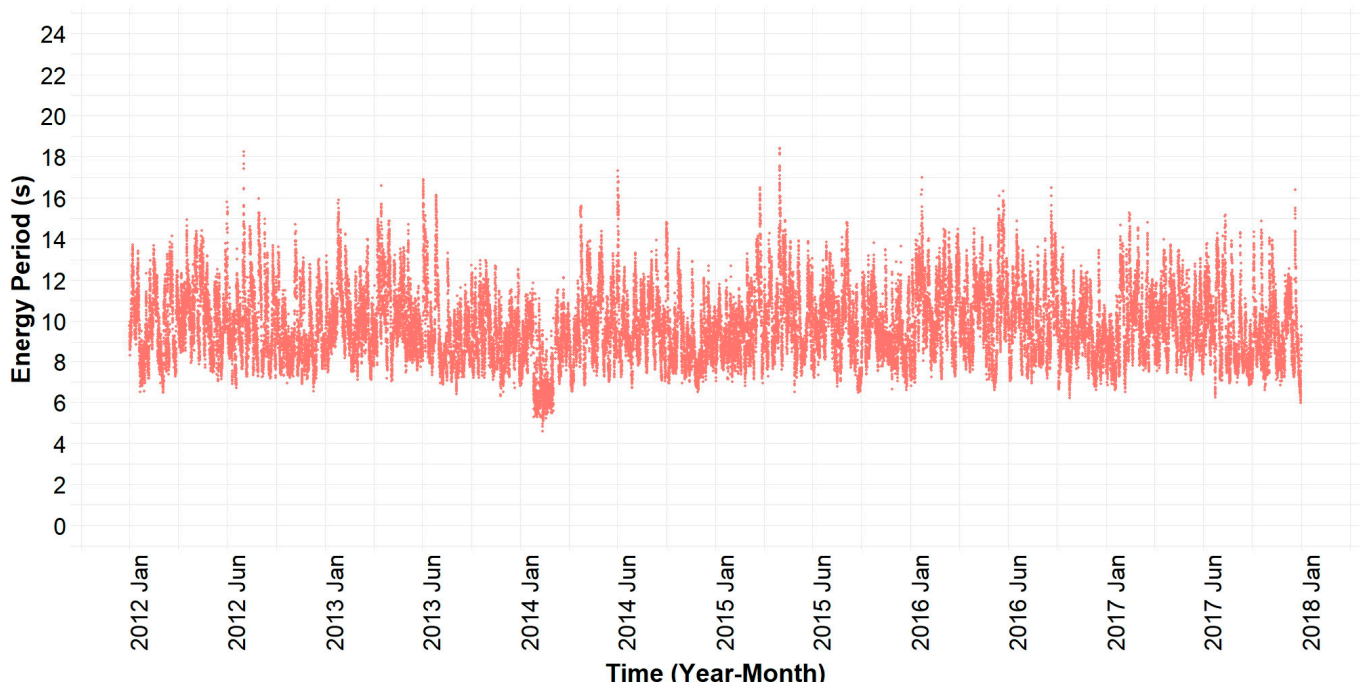


Figure 2. Time series of the energy period calculated based on spectral data from Buoy 32012 in the Peru Basin.

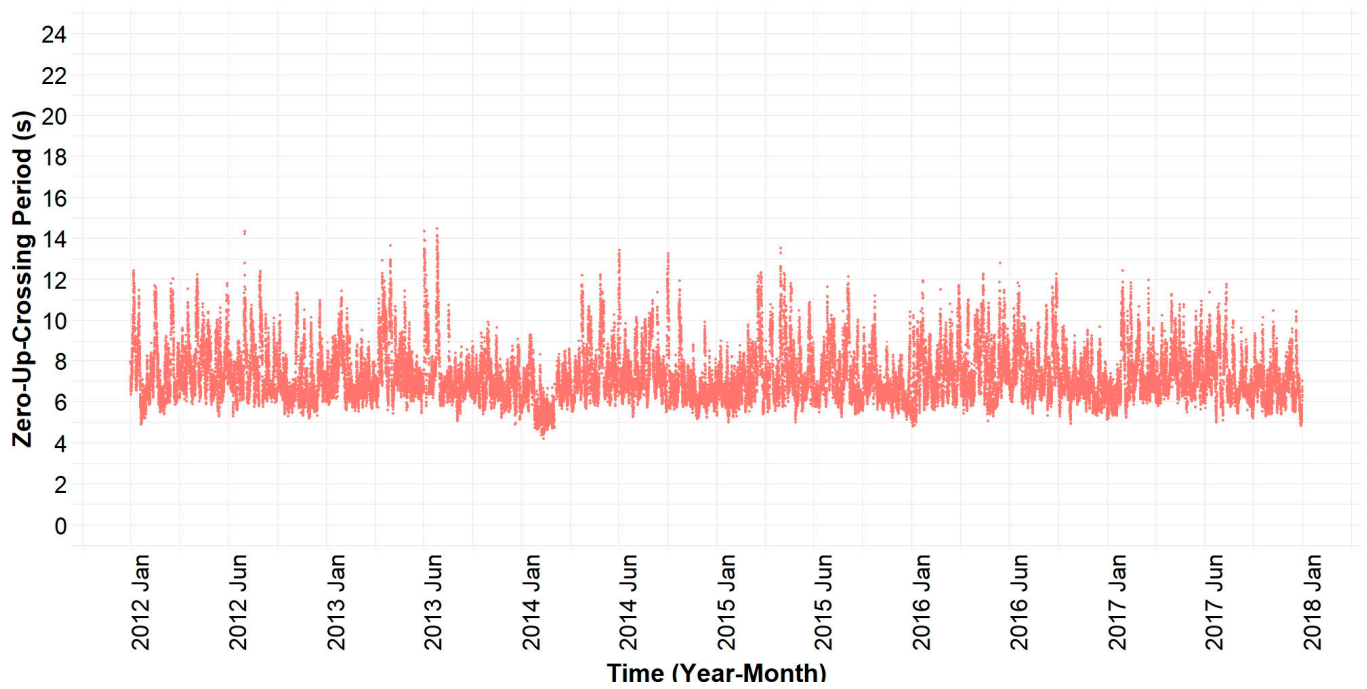


Figure 3. Time series of the zero-up-crossing period calculated based on spectral data from Buoy 32012 in the Peru Basin.

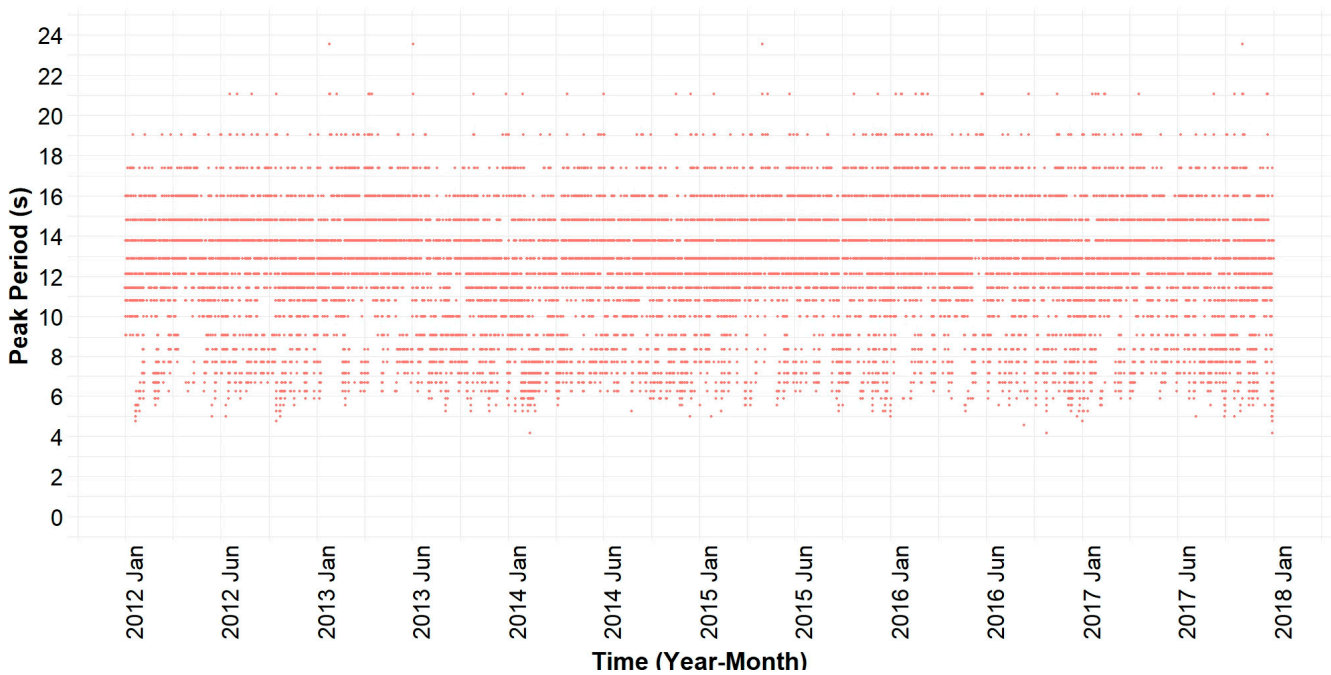


Figure 4. Time series of the peak period taken from the sea state wave spectrums of Buoy 32012 in the Peru Basin.

3.2. Analysis of the Energy Period Calculation Using Diverse Approximations

As commented in Section 2.3, T_e and spectral data are not always released by the buoy administrators, so diverse approximations for T_e have been modelled to overcome this issue.

Figure 5 shows a scatter plot of T_e calculated using the spectral moments, Equation (1), versus the Bretschneider T_z approximation, Equation (8). Even they can be correlated by linear regression, mostly the Bretschneider T_z approximation under estimate T_e . Figure 6 presents the Bretschneider T_z approximation error, showing that the maximum errors exceed 25% (underestimation). If this calculation is carried out assuming the JONSWAP T_z approximation used by [35–37], higher underestimation errors are expected.

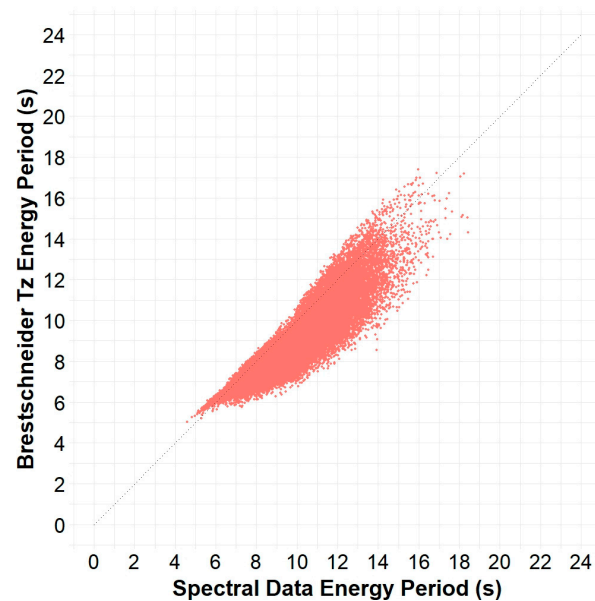


Figure 5. Scatter plot of energy period, spectral data versus Bretschneider T_z , from Buoy 32012 in the Peru Basin.

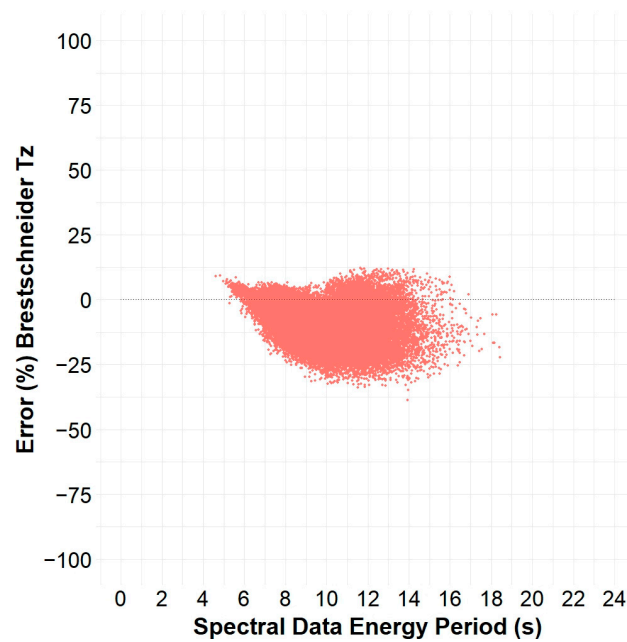


Figure 6. Approximation error of Bretschneider T_z energy period from Buoy 32012 in the Peru Basin.

Figure 7 shows the scatter plot of the energy period calculated using the spectral data versus that calculated using the NCC T_z approximation, Equation (10). In contrast to the previous Bretschneider T_z approximation, the NCC T_z approximation presents some more overestimation. Figure 8 presents its approximation error showing maximum errors also higher than 25% (underestimation).

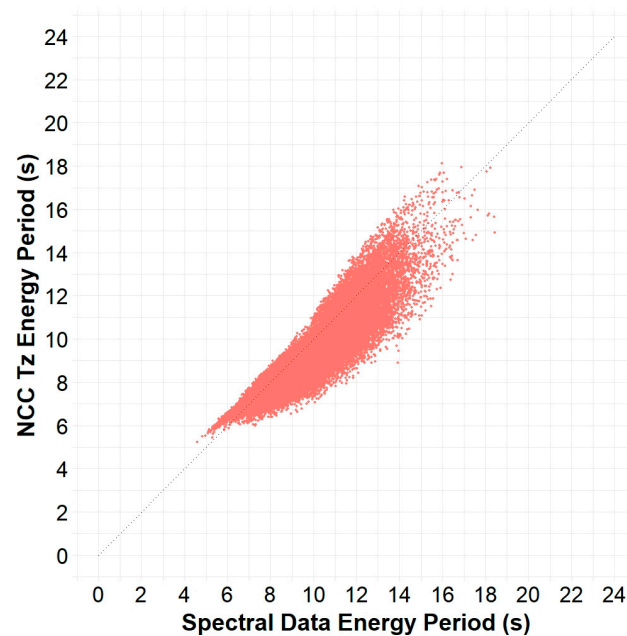


Figure 7. Scatter plot of energy period, spectral data versus NCC T_z , from Buoy 32012 in the Peru Basin.

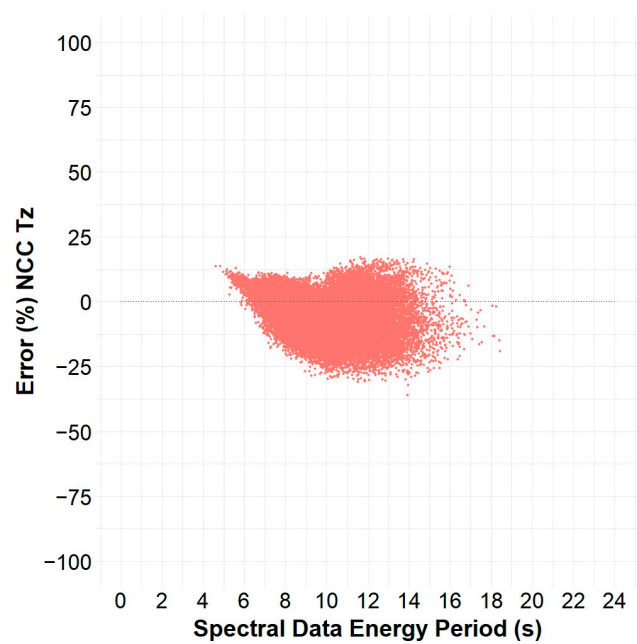


Figure 8. Approximation error of NCC T_z energy period from Buoy 32012 in the Peru Basin.

Contrary to approximate T_e from T_z , utilising T_p generates unrealistic results. Figure 9 presents a scatter plot of the T_e computed from the spectral data versus those using the NCC T_p approximation, Equation (9). Besides that, most of the results overestimate; they present a strong mark of the buoy measurement frequency. Figure 10 shows the approximation error of the NCC T_p correlation, presenting surprising errors higher than 100% (overestimation).

Carrying out the same exercise for the other correlations that use T_p , Equations (6) and (7), they generated similar behaviour for the results and worse errors (the JONSWAP T_p correlation presents errors of almost 125%). Thus, this analysis allows us to state that correlations that use T_p to approximate T_e are not recommendable.

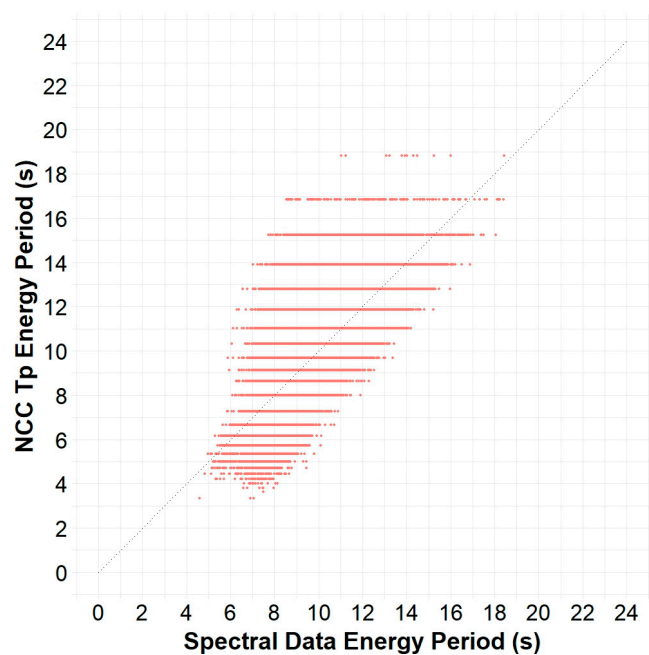


Figure 9. Scatter plot of energy period, spectral data versus NCC T_p , from Buoy 32012 in the Peru Basin.

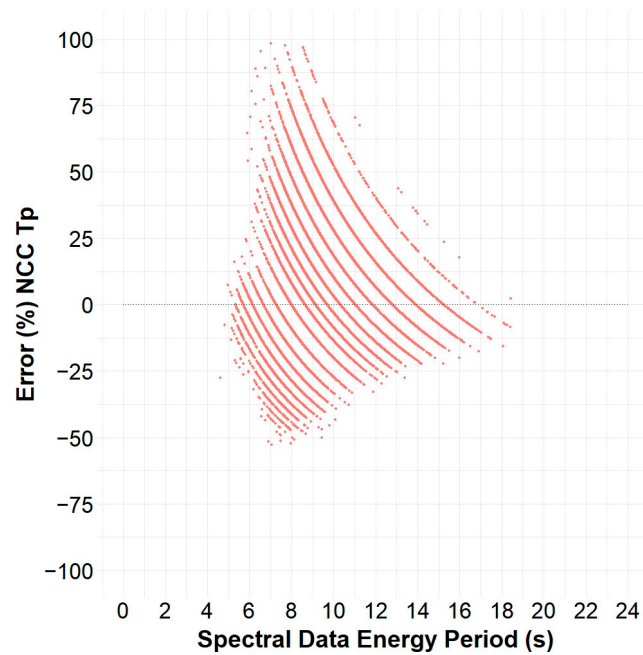


Figure 10. Approximation error of NCC T_p energy period from Buoy 32012 in the Peru Basin.

3.3. A Kernel T_z Approximation for the Peru Basin

T_z was again used to approximate T_e , but this time utilising a Kernel regression, as presented in Section 2.4. T_e and T_z computed using the spectral moments, Equations (1) and (2), were used for the training data x_i and y_i , respectively. A sequence from 0 to 24 s spaced by 0.001 s was used for the vector x . A value equal to 0.3 was selected for h after a tuning process. Once the Kernel regression process was concluded, a Kernel “coefficient” sequence was calculated by dividing the estimated Y by its respective x . Figure 11 shows the resulting Kernel “coefficient” curve. An almost linear behaviour of the Kernel “coefficient” corresponding to a range from 1.16 to 1.35 is noted from the figure. The Bretschneider and NCC coefficients to approximate T_e from T_z , Equations (8) and (10), respectively, were located in that range. Moreover, less than 16% of T_z calculated based on the spectral data were inside that linear range (from 8.5 s to 13 s).

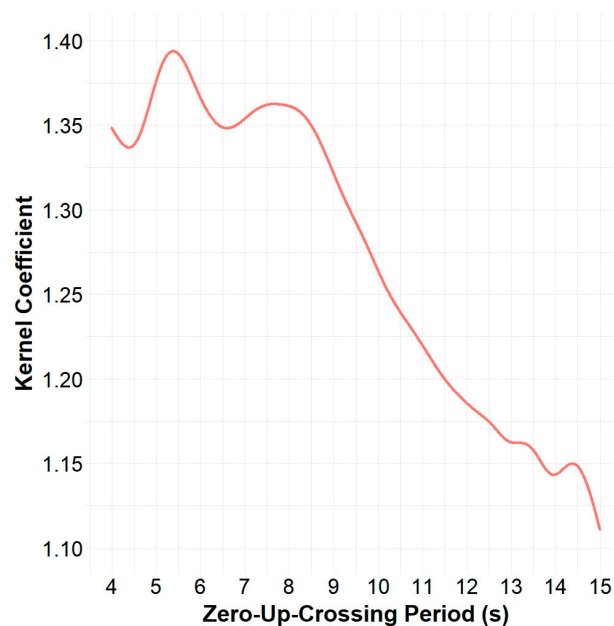


Figure 11. The Kernel “coefficient” curve for the Peru Basin.

Figure 12 presents a scatter plot of T_e calculated using the spectral data versus T_e calculated using the Kernel “coefficient” curve. In contrast to the Bretschneider and NCC approximations using T_z , the energy periods were better distributed side by side with the symmetric axis. The error generated by this Kernel regression is shown in Figure 13. Similarly, the values were more uniformly distributed around the axis of errors equal to zero. Most errors were lower than 25%, over and underestimation.

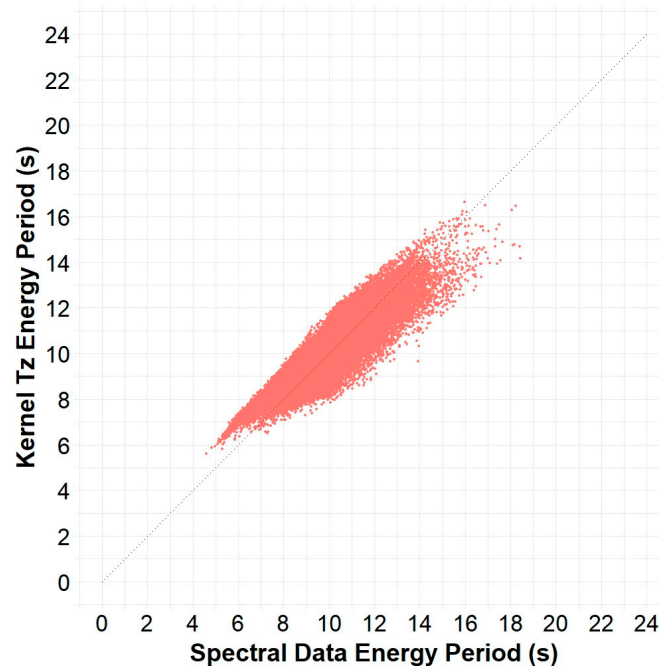


Figure 12. Scatter plot of energy period, spectral data versus Kernel T_z , from Buoy 32012 in the Peru Basin.

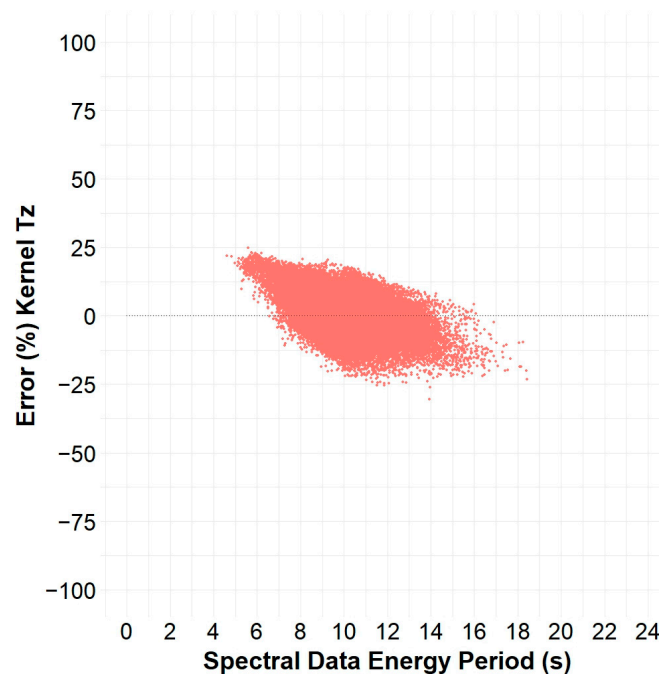


Figure 13. Approximation error of Kernel T_z energy period from Buoy 32012 in the Peru Basin.

In summary, the maximum error generated by each of the diverse approximations of T_e is presented in Table 2. The lowest errors were those generated by the approximations based on T_z , which underpredicted T_e . The Kernel T_z produced the best estimation of T_e .

In contrast, the highest errors were those generated by the correlations based on T_p , with shocking errors higher than 100%. As the table shows, the maximum errors occurred when estimates of two well-defined T_e were tried with the approximations based on T_z for T_e equal to 13.9 and T_p for T_e equal to 7.0. Those situations happened at the end of 2017.

Table 2. Maximum percentage error generated by each of the diverse approximations of T_e . The table also presents the T_e estimated and the date and time of occurrence taken from the spectral data of Buoy 32012 in the Peru Basin.

Approximation	Maximum Error (%)	Spectral T_e (s)	When DD/MM/YEAR HH:MM
Kernel T_z	−30.6	13.9	02/11/2017 14:00
NCC T_z	−36.0	13.9	02/11/2017 14:00
Bretschneider T_z	−38.6	13.9	02/11/2017 14:00
NCC T_p	98.4	7.0	29/12/2017 04:00
Bretschneider T_p	112.5	7.0	29/12/2017 04:00
JONSWAP T_p	120.7	7.0	29/12/2017 04:00

3.4. Analysis of Temporal Variability

In this subsection, an analysis of the wave climate and the temporal variability regarding T_e is carried out for monthly and seasonal time scales.

3.4.1. Monthly Time Scale

Figure 14 shows the monthly distribution of average T_e and CV calculated using the spectral moments (Equations (1) and (14)). Their numerical values are at the top, with CV in brackets. As the figure shows, the monthly average of T_e started growing in January, reaching its highest value in May (10.7 s), then decreasing up to November (9.2 s). Based on this monthly distribution, an annual average of T_e equal to 9.8 s could be calculated, as shown in Table 3.

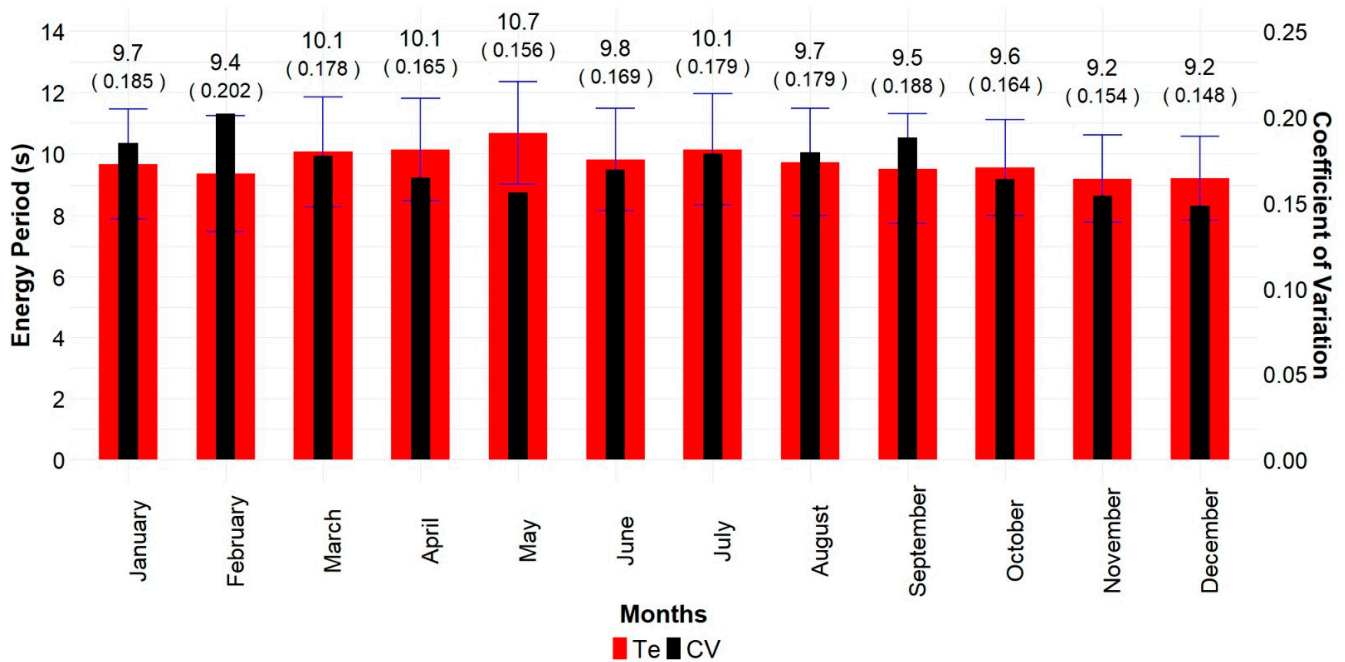


Figure 14. Monthly average of the energy period, standard deviation (blue) and coefficient of variation using spectral data from Buoy 32012 in the Peru Basin. Numerical values are at the top, and CV is in brackets.

Table 3. Annual average, extreme values and error percentage from calculating the monthly average of energy period using spectral data and diverse approximations for Buoy 32012 in the Peru Basin.

Approximation	Annual	Maximum		Minimum	
	T_e (s)/Error (%)	T_e (s)/Error (%)	Month	T_e (s)/Error (%)	Month
Spectral Data	9.8	10.7	May	9.2	November
Kernel T_z	0.0	-0.7	May	-0.5	December
NCC T_z	-6.9	-6.5	May	-8.4	December
Bretschneider T_z	-10.7	-10.2	May	-12.0	December
NCC T_p	3.3	0.7	May	5.4	August
Bretschneider T_p	10.7	7.8	May	12.9	August
JONSWAP T_p	14.9	12.0	May	17.3	August

This analysis was also carried out using the diverse approximations for T_e , also summarised in Table 3. For T_e 's annual average and extreme values (maximum and minimum), Kernel T_z presented the best results, followed by NCC T_p and NCC T_z approximations. The highest errors were from the approximations using the traditional Bretschneider and JONSWAP correlations. Again, the approximations based on T_z underpredicted the results, and those based on T_p overpredicted. It is worth pointing out that the NCC approximations were linear regressions adjusted to actual data, in contrast to the Bretschneider and JONSWAP coefficients calculated from idealised spectrums.

Based on the spectral data, May was computed as the month with the maximum T_e , and each of the diverse approximations was able to reproduce it. On the other hand, the calculations for the month for the minimum T_e were divided into two groups: one consisting of those based on T_z , calculating December as the month with the lowest T_e , the month close to November as computed by the spectral data; and the other, consisting of those based on T_p , computing for August as the month with the lowest T_e .

Regarding the monthly distribution of average CV (Figure 14), it grew quickly from the beginning of the year and reached its maximum value (0.202) in February. Then, it trended down and up again, reaching a new peak in September, and then declined to its lowest value (0.148) in December. From this distribution of CV, computed based on spectral data, an annual CV was calculated to be equal to 0.172, as shown in Table 4. This annual CV indicated that T_e could be considered statistically stable.

Table 4. Annual average, extreme values and error percentage from calculating the monthly average of coefficient of variation using spectral data and diverse approximations for Buoy 32012 in the Peru Basin.

Approximation	Annual	Maximum		Minimum	
	CV/ Error (%)	CV/ Error (%)	Month	CV/ Error (%)	Month
Spectral Data	0.172	0.202	February	0.148	December
Kernel T_z	-15.2	-16.0	January	-17.2	November
NCC T_z	-1.9	-3.5	January	-8.8	November
Bretschneider T_z	-1.9	-3.5	January	-8.8	November
NCC T_p	36.0	26.1	September	13.4	May
Bretschneider T_p	36.0	26.1	September	13.4	May
JONSWAP T_p	36.0	26.1	September	13.4	May

The capability of the diverse approximations of T_e to compute the previous values for CV was also tested. Table 4 shows that the Kernel T_z was not the best this time because a Kernel regression is a numerical smoother trying to approximate the best average value, losing information about the data dispersion. The best approximation was obtained by the correlations based on T_z because this is an actual physical characterisation of wave periods. One more time, the highest errors were computed by the correlation based on T_p , which is dependent on the buoy measurement frequency. For the extreme values, the correlations based on T_z computed the months close to those computed by the spectral data. In contrast, the correlations based on T_p calculated faraway months.

Figure 15 presents the generated error percentage for each month when comparing results from the spectral data versus those using the diverse approximations for the calculation of T_e . In general, the approximations using T_p overestimated the results, and those using T_z underestimated, except for Kernel T_z . The best results were calculated using the Kernel T_z approximation. It presented a maximum error equal to 2.1% in August. It started underestimating at the beginning of the year, except in February, then overestimated from June to September, and then underestimated for the rest of the year.

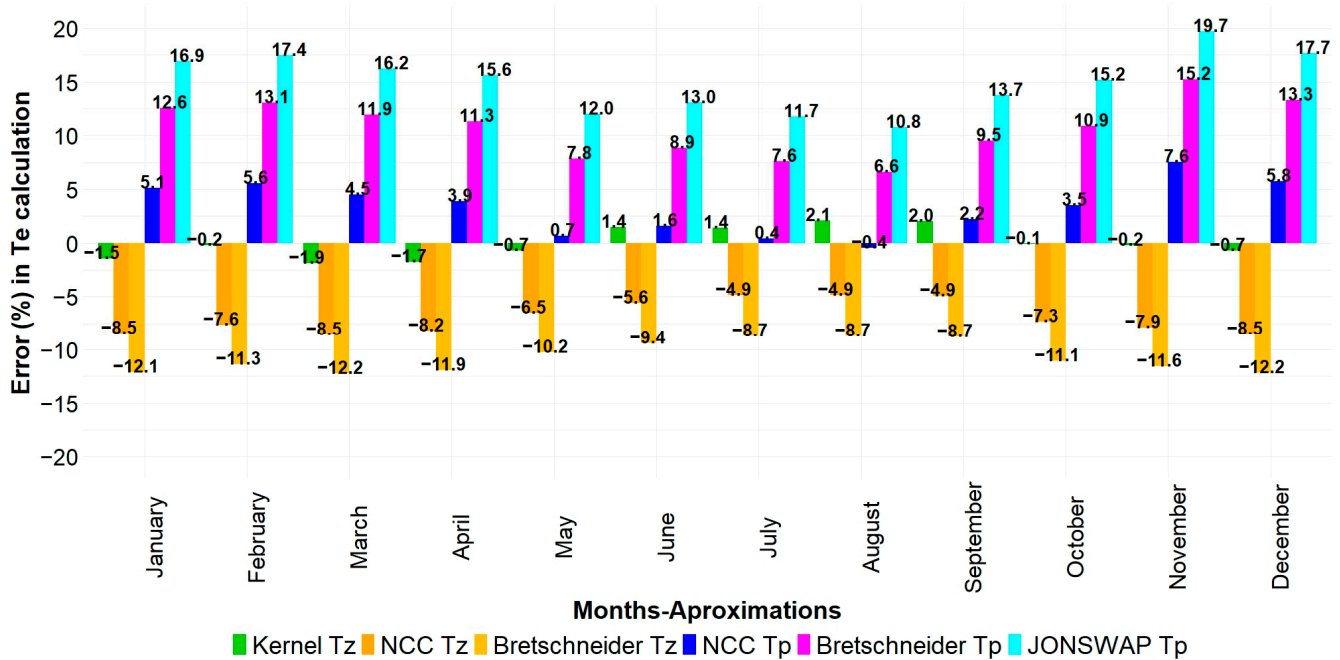


Figure 15. Error percentage in calculating the monthly average of energy period using the diverse approximations.

Table 5 presents the maximum and minimum errors generated by each approximation. After the Kernel T_z approximation, those using the NCC coefficients generated the best results. The NCC T_p approximation generated the following, better, results, even using T_p . Significant high errors were those generated by the traditional Bretschneider and JONSWAP correlations, with the highest error generated by the JONSWAP approximation. Aside from the Kernel regression, the months in the table were divided into two groups. They were the months calculated from the correlations based on T_z and those based on T_p . There was an exception for the minimum error calculated by NCC T_p . For this approximation, the results showed its absolute values close to 0.4% for July and August.

Table 5. Maximum and minimum error percentage in calculating the monthly average of energy period using the diverse approximations.

Approximation	Maximum		Minimum	
	Error (%)	Month	Error (%)	Month
Kernel T_z	2.1	August	-0.1	October
NCC T_z	-8.5	March	-4.9	July
Bretschneider T_z	-12.2	March	-8.7	July
NCC T_p	7.6	November	0.4	July
Bretschneider T_p	15.2	November	6.6	August
JONSWAP T_p	19.7	November	10.8	August

Figure 16 presents the monthly distribution of the error percentage for calculating the monthly average of CV for each of the diverse approximations of T_e . The results could

be divided into three groups. First was the smoother Kernel regression, which lost the randomness of the wave period, so it was not able to give the best results, even being based on T_z . Second, the approximations based on T_z gave the best results due to the physical representation of wave periods captured by T_z , including their randomness. The last group included the approximations based on T_p that generated impressive errors due to the T_p dependence on the buoy frequency of measurements. This situation is reflected in Table 6, where the maximum and minimum errors for each T_e approximation are presented with the respective month of occurrence. Again, aside from the Kernel regression, these months were divided into two groups based on T_z or T_p for the calculation of T_e .

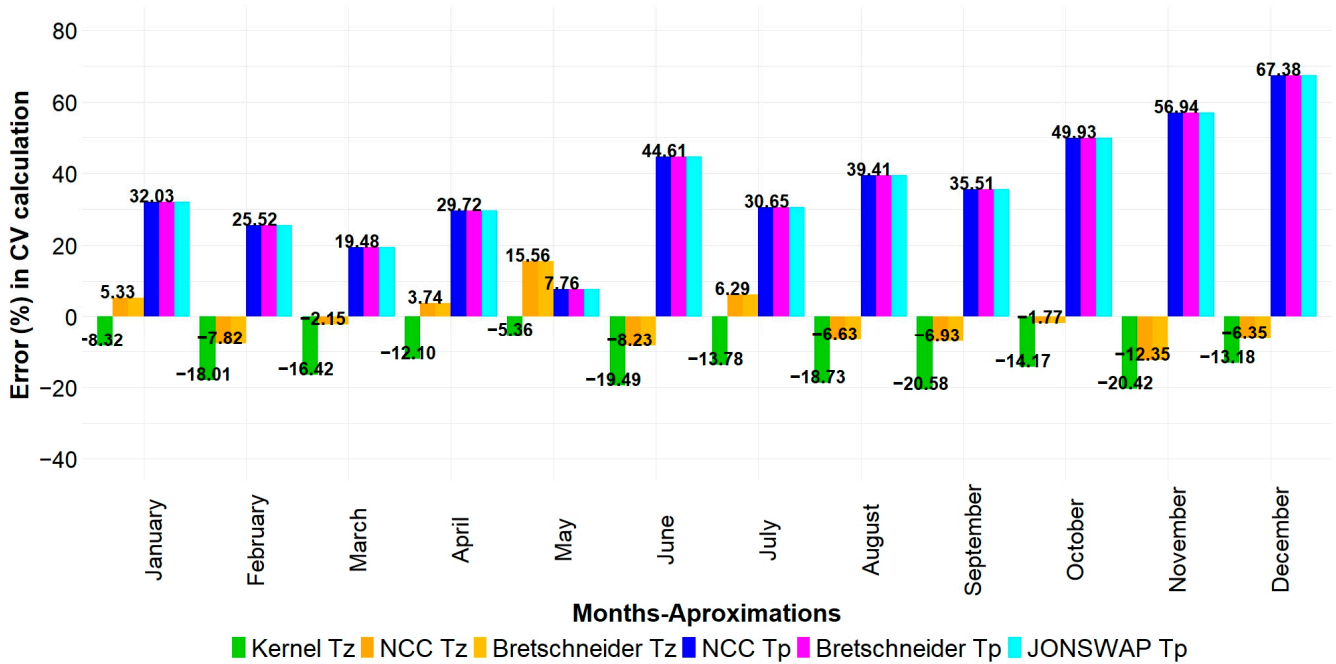


Figure 16. Error percentage in calculating the monthly average of coefficient of variation using the diverse approximations.

Table 6. Maximum and minimum error percentage in calculating the monthly average of coefficient of variation using the diverse approximations.

Approximation	Maximum		Minimum	
	Error (%)	Month	Error (%)	Month
Kernel T_z	-20.6	September	-5.4	May
NCC T_z	15.6	May	-1.8	October
Bretschneider T_z	15.6	May	-1.8	October
NCC T_p	67.4	December	7.8	May
Bretschneider T_p	67.4	December	7.8	May
JONSWAP T_p	67.4	December	7.8	May

3.4.2. Seasonal Time Scale

Figure 17 shows the seasonal distribution of T_e and CV. T_e 's high values were in the middle of the year, with the highest in autumn (10.2 s). The low values of T_e were at the beginning and end of the year, with the lowest in spring (9.4 s). From the seasonal distribution of T_e , an annual average could be calculated, equal to 9.8 s. Regarding CV, the highest variability was presented in summer (0.187), and the lowest in spring (0.163). Similarly, an annual average CV equal to 0.175 was estimated from this CV distribution. The average seasonal distribution of CV indicated that T_e had stable seasonal behaviour throughout the year. These seasonal results were consistent with the monthly distribution of T_e and CV, as shown in Figure 14.

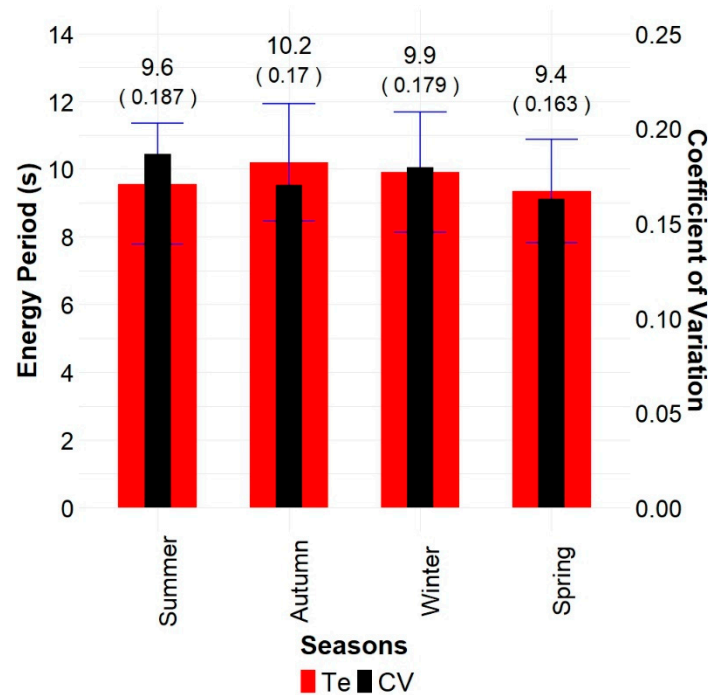


Figure 17. Seasonal average of energy period, standard deviation (blue) and coefficient of variation using spectral data from Buoy 32012 in the Peru Basin. Numerical values are at the top, and CV is in brackets.

This analysis was also carried out with each of the diverse approximations of T_e . A summary is presented in Tables 7 and 8, showing the annual average, extreme values, and errors from each diverse approximations. The Kernel regression calculated the best results for T_e 's annual average and extreme values, followed by the NCC correlation. The highest errors were calculated by the traditional Bretschneider and JONSWAP correlations. For the extreme values, the seasons presented in the table were consistent with those shown in Table 4, except for the season of the minimum T_e calculated by the T_p approximations. The results for T_p indicated a minimum T_e close to 11 s for spring and winter.

Table 7. Annual average, extreme values and error percentage from calculating the seasonal average of energy period using spectral data and the diverse approximations for Buoy 32012 in the Peru Basin.

Approximation	Annual	Maximum		Minimum	
	T_e (s)/Error (%)	T_e (s)/Error (%)	Season	T_e (s)/Error (%)	Season
Spectral Data	9.8	10.2	Autumn	9.4	Spring
Kernel T_z	0.0	-0.6	Autumn	-0.1	Spring
NCC T_z	-7.0	-7.0	Autumn	-7.6	Spring
Bretschneider T_z	-10.7	-10.7	Autumn	-11.3	Spring
NCC T_p	3.3	2.1	Autumn	5.2	Spring
Bretschneider T_p	10.7	9.4	Autumn	12.7	Spring
JONSWAP T_p	14.9	13.6	Autumn	17.1	Spring

Regarding CV, Table 8, the approximations based on T_z calculated the best results due to the physical characteristic of T_z . The Kernel regression was not able to manage that because it was a smoother regression, and those based on the “imposed” T_p calculated the highest errors. It is said to be “imposed” due to the predefined measurement frequency of the buoy. For the extreme values, the seasons presented in Table 8 were consistent with the months presented for the extreme values in Table 4.

Table 8. Annual average, extreme values and error percentage from calculating the seasonal average of coefficient of variation using spectral data and the diverse approximations for Buoy 32012 in the Peru Basin.

Approximation	Annual	Maximum		Minimum	
	CV/ Error (%)	CV/ Error (%)	Season	CV/ Error (%)	Season
Spectral Data	0.175	0.187	Summer	0.163	Spring
Kernel T_z	-14.9	-14.0	Summer	-16.5	Spring
NCC T_z	-1.4	-2.4	Summer	-5.9	Spring
Bretschneider T_z	-1.4	-2.4	Summer	-5.9	Spring
NCC T_p	35.0	32.1	Spring	27.9	Autumn
Bretschneider T_p	35.0	32.1	Spring	27.9	Autumn
JONSWAP T_p	35.0	32.1	Spring	27.9	Autumn

Figure 18 presents the seasonal distribution of the error percentage generated by each approximation of T_e compared to those using the spectral data, Figure 17. Again, without considering the Kernel regression, the approximations based on T_z underestimated the results, and those using T_p overestimated. The best result was that generated by the Kernel regression, with the highest error lower than 2% for winter. The Kernel regression overestimated in winter and underestimated in the other seasons.

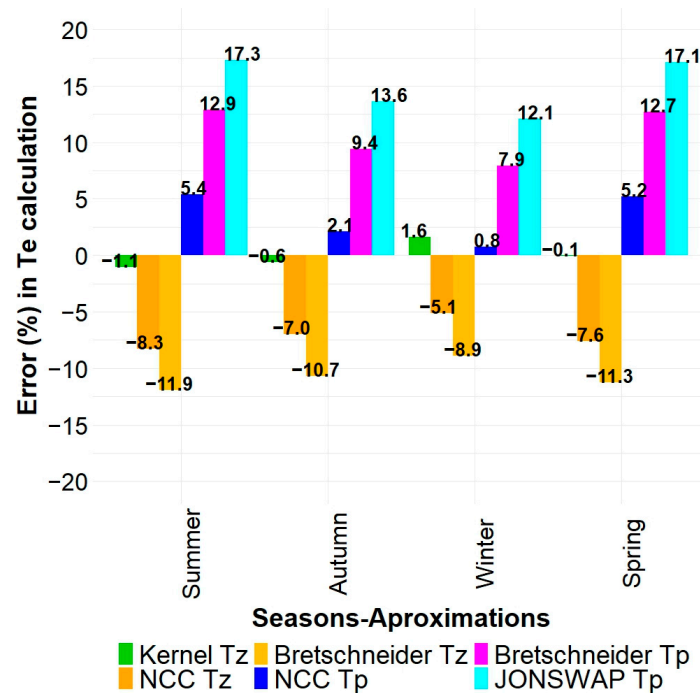


Figure 18. Error percentage in calculating the seasonal average of energy period using the diverse approximations.

Table 9 presents the seasonal maximum and minimum error percentages generated by the diverse approximations of T_e when compared against that using the spectral data, Figure 17. After the Kernel regression, the approximation that generated the best results was the NCC T_p , even better than those using T_z . The highest errors were computed by the traditional Bretschneider and JONSWAP approximations. These error percentages, their seasonal distribution, and the maximum and minimum error seasons were consistent with the monthly time scale results, Figure 15 and Table 5. There was an exception for the maximum error; summer and spring presented close values for the approximations based on T_p .

Table 9. Maximum and minimum error percentages in calculating the seasonal average of energy period using the diverse approximations.

Approximation	Maximum		Minimum	
	Error (%)	Season	Error (%)	Season
Kernel T_z	1.6	Winter	−0.1	Spring
NCC T_z	−8.3	Summer	−5.1	Winter
Bretschneider T_z	−11.9	Summer	−8.9	Winter
NCC T_p	5.4	Summer	0.8	Winter
Bretschneider T_p	12.9	Summer	7.9	Winter
JONSWAP T_p	17.3	Summer	12.1	Winter

Figure 19 presents the seasonal distribution of error percentages for calculating CV by each of the approximations of T_e . As in the case of the monthly time scale, they were divided into three groups: the approximation based on the Kernel regression, those based on T_z , and those based on T_p . The best result was calculated by the approximations based on T_z due to its physical representation of the randomness of the wave periods. It was followed by the Kernel regression, which smoothed the data dispersion, and the highest error was calculated by the approximations based on the “imposed” T_p .

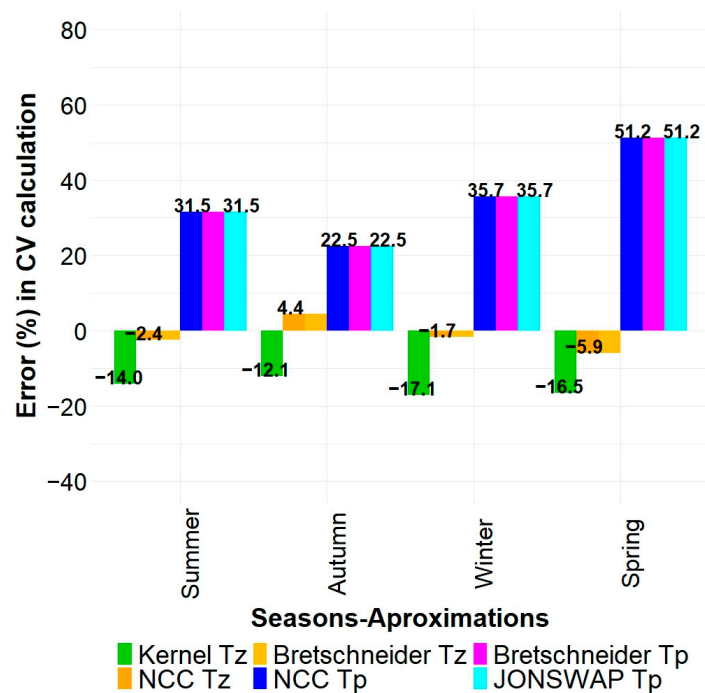


Figure 19. Error percentages in calculating the seasonal average of coefficient of variation using the diverse approximations.

The maximum and minimum errors of the seasonal distribution of CV by each approximation of T_e are presented in Table 10. The three groups of errors explained above are also reflected there. The seasons for the maximum and minimum errors followed the months presented in Table 6, monthly time scale, except for the approximations based on T_z .

Table 10. Maximum and minimum error percentages in calculating the seasonal average of coefficient of variation using the diverse approximations.

Approximation	Maximum		Minimum	
	Error (%)	Season	Error (%)	Season
Kernel T_z	-17.1	Winter	-12.1	Autumn
NCC T_z	-5.9	Spring	-1.7	Winter
Bretschneider T_z	-5.9	Spring	-1.7	Winter
NCC T_p	51.2	Spring	22.5	Autumn
Bretschneider T_p	51.2	Spring	22.5	Autumn
JONSWAP T_p	51.2	Spring	22.5	Autumn

3.4.3. Annual Time Scale

Table 11 summarises the annual averages of T_e and CV taken from the temporal variability time scales, monthly from Tables 3 and 4 and seasonal from Tables 7 and 8, which presented consistent results.

Table 11. Annual average of energy period and coefficient of variation taken from the monthly and seasonal time scale analysis using spectral data from Buoy 32012 in the Peru Basin.

Period	T_e (s)	CV
Monthly	9.8	0.172
Seasonal	9.8	0.175

In order to double-check in these last results, an annual average was computed using all of the spectral data for the selected years, no longer by monthly or seasonal time scales. Table 12 shows these results, which are consistent with those in Table 11. Therefore, a T_e equal to 9.8 s could characterise the Peru Basin, which can also be considered stable, as its CV is lower than 2%.

Table 12. Annual average of energy period and coefficient of variation by spectral data and the diverse approximations from Buoy 32012 in the Peru Basin.

Approximation	T_e (s)/ Error (%)	CV/ Error (%)
Spectral Data	9.8	0.178
Kernel T_z	0.0	-14.0
NCC T_z	-6.9	-0.1
Bretschneider T_z	-10.7	-0.1
NCC T_p	3.3	32.8
Bretschneider T_p	10.6	32.8
JONSWAP T_p	14.9	32.8

Table 12 also presents the error percentages for T_e and CV calculated using the diverse approximations. Again, the best result was obtained using the Kernel regression for calculating the average T_e . The NCC correlations followed it, and the traditional Bretschneider and JONSWAP approximations generated the highest errors. Similarly, for the average CV, the correlations based on T_z , except the Kernel regression, captured very well the original data dispersion that represented the variability, in contrast to the Kernel smoother and the correlations based on the “imposed” T_p .

3.5. Analysis of the Monthly and Seasonal Variability

Table 13 presents the results of the monthly variability of T_e characterised by MV. According to the results from the spectral data, T_e can be considered stable, as its MV is lower than 2%. Even so, the longest T_e occurred in May, and the shortest in November.

The best approximation was calculated by the Kernel T_z regression, with a percentage error lower than 2%. However, it calculated December as the month with the lowest T_e , compared to November computed from the spectral data. This was because the Kernel T_z regression slightly underpredicted the minimum T_e in the subsequent month.

Table 13. Monthly variability index, error percentage, maximum, minimum, and annual average energy period by spectral data and the diverse approximations from Buoy 32012 in the Peru Basin.

Approximation	Maximum		Minimum		Annual	MV/
	T_e (s)	Month	T_e (s)	Month	T_e (s)	Error (%)
Spectral Data	10.7	May	9.2	November	9.8	0.153
Kernel T_z	10.6	May	9.1	December	9.8	-1.9
NCC T_z	10.0	May	8.4	December	9.1	12.9
Bretschneider T_z	9.6	May	8.1	December	8.7	12.9
NCC T_p	10.8	May	9.7	August	10.1	-30.7
Bretschneider T_p	11.5	May	10.4	August	10.8	-30.7
JONSWAP T_p	12.0	May	10.8	August	11.2	-30.7

Besides the Kernel T_z regression, the other approximations for T_e were based on linear tuning of T_z and T_p . Thus, for this analysis, no differences in their results were expected within the groups of approximations using T_z and T_p . The approximations based on T_z calculated the minimum T_e for December, and these based on T_p calculated the minimum T_e for August. Conversely, all of the diverse approximations calculated May as the month with the maximum T_e . Moreover, the approximations based on T_z had the best results after the Kernel T_z regression. On the other hand, the highest errors were calculated for the approximations based on T_p . Contrary to the T_e variability analysis explained in Section 3.4, the approximations based on T_z overestimated, and those based on T_p underestimated the results.

Table 14 presents the results of the seasonal variability analysis of T_e represented by its SV. The variability of T_e could be considered stable, as its SV was lower than 2%, according to the calculations using the spectral data. The maximum seasonal T_e was estimated for autumn, and the minimum for spring. The diverse approximations successfully reproduced these results. However, comparing with the monthly variability of T_e , Table 13, the approximations based on T_p computed the minimum T_e for August, that is, for winter.

Table 14. Seasonal variability index, error percentage, maximum, minimum, and annual average energy period by spectral data and the diverse approximations from Buoy 32012 in the Peru Basin.

Approximation	Maximum		Minimum		Annual	SV/
	T_e (s)	Season	T_e (s)	Season	T_e (s)	Error (%)
Spectral Data	10.2	Autumn	9.4	Spring	9.8	0.087
Kernel T_z	10.1	Autumn	9.3	Spring	9.8	-6.3
NCC T_z	9.5	Autumn	8.6	Spring	9.1	7.2
Bretschneider T_z	9.1	Autumn	8.3	Spring	8.7	7.2
NCC T_p	10.4	Autumn	9.8	Spring	10.1	-34.4
Bretschneider T_p	11.2	Autumn	10.5	Spring	10.8	-34.4
JONSWAP T_p	11.6	Autumn	10.9	Spring	11.2	-34.4

Once more, the Kernel T_z regression calculated the best results, followed by the approximations based on T_z , and the approximations based on T_p generated the highest errors. Similarly to the monthly variability index, the approximations based on T_z overestimated, besides the Kernel T_z regression, and those based on T_p underestimated the results.

4. Conclusions

The question of what is the best estimation for T_e at conditions different from those of the Northern Hemisphere was discussed in this paper. Spectral data from a buoy in the Peru Basin were used for this assessment. The linear relationships based on the traditional Bretschneider and JONSWAP standard wave spectrums generated substantially high errors. This situation indicates that they are unsuitable for conditions of open water and unlimited fetch, which characterise offshore regions of the South Pacific, such as the Peru Basin. Additionally, the linear relationships based on local calibration coefficients generated acceptable errors. However, one of their relationships was based on T_p , which, according to this analysis, does not resemble the physics of ocean wave periods because it relies on the frequency of buoy measurements.

On the other hand, this work proposed an approximation for T_e based on a Kernel regression, presenting a Kernel “coefficient” curve. This Kernel approximation generated negligible errors for the calculation of average T_e . Moreover, this work found that less than 16% of the T_z time series, calculated based on spectral data, were in the linear region of the Kernel curve. The coefficients of the linear relationships based on T_z were located in this region. Even so, this work showed that for calculating the variability of T_e , the best CV results were calculated by the correlation based on T_z because it represented the actual wave period, including its randomness. However, if the variability has to be calculated using the variability index, the proposed approximation based on the Kernel regression generated the lowest error.

Based on the spectral data, T_e and CV monthly and seasonal distributions computed a stable T_e annual average equal to 9.8 s. In future work, a similar analysis regarding the impact of the diverse approximations of T_e , including the proposal based on the Kernel regression, can be carried out for the assessment of wave power.

Author Contributions: Conceptualisation, D.D.L.T.; methodology, D.D.L.T. and A.O.; validation, D.D.L.T.; formal analysis, D.D.L.T. and A.O.; investigation, D.D.L.T. and A.O.; writing—original draft preparation, D.D.L.T.; writing—review and editing, D.D.L.T., J.L. and A.O.; supervision, J.L. and A.O. All authors have read and agreed to the published version of the manuscript.

Funding: This research received no external funding.

Institutional Review Board Statement: Not applicable.

Informed Consent Statement: Not applicable.

Data Availability Statement: The spectral data used in this work can be collected from the website of NDBC [26]. Data generated in this work are available from the corresponding author upon request.

Conflicts of Interest: The authors declare no conflict of interest.

References

1. Reikard, G.; Pinson, P.; Bidlot, J.R. Forecasting Ocean Wave Energy: The ECMWF Wave Model and Time Series Methods. *Ocean Eng.* **2011**, *38*, 1089–1099. [[CrossRef](#)]
2. Iglesias, G.; López, M.; Carballo, R.; Castro, A.; Fraguera, J.A.; Frigaard, P. Wave Energy Potential in Galicia (NW Spain). *Renew. Energy* **2009**, *34*, 2323–2333. [[CrossRef](#)]
3. Ribeiro, A.S.; deCastro, M.; Rusu, L.; Bernardino, M.; Dias, J.M.; Gomez-Gesteira, M. Evaluating the Future Efficiency of Wave Energy Converters along the NW Coast of the Iberian Peninsula. *Energies* **2020**, *13*, 3563. [[CrossRef](#)]
4. Lenee-Bluhm, P.; Paasch, R.; Özkan-Haller, H.T. Characterizing the Wave Energy Resource of the US Pacific Northwest. *Renew. Energy* **2011**, *36*, 2106–2119. [[CrossRef](#)]
5. López, M.; Veigas, M.; Iglesias, G. On the wave energy resource of Peru. *Energy Convers. Manag.* **2015**, *90*, 34–40. [[CrossRef](#)]
6. Wu, S.; Liu, C.; Chen, X. Offshore Wave Energy Resource Assessment in the East China Sea. *Renew. Energy* **2015**, *76*, 628–636. [[CrossRef](#)]
7. Cornett, A.M. Inventory of Canada’s Offshore Wave Energy Resources. In Proceedings of the 25th International Conference on Offshore Mechanics and Arctic Engineering, Hamburg, Germany, 4 June 2006. [[CrossRef](#)]

8. Beels, C.; De Rouck, J.; Verhaeghe, H.; Geeraerts, J.; Dumon, G. Wave Energy on the Belgian Continental Shelf. In Proceedings of the OCEANS 2007—Europe, Aberdeen, UK, 18 June 2007. [CrossRef]
9. Cornett, A.M. A Global Wave Energy Resource Assessment. In Proceedings of the Eighteenth International Offshore and Polar Engineering Conference, Vancouver, BC, Canada, 6 July 2008.
10. Li, N.; Garcia-Medina, G.; Cheung, K.F.; Yang, Z. Wave energy resources assessment for the multi-modal sea state of Hawaii. *Renew. Energy* **2021**, *174*, 1036–1055. [CrossRef]
11. Cahill, B.G.; Lewis, T. Wave Energy Resource Characterisation of the Atlantic Marine Energy Test Site. *Int. J. Mar. Energy* **2013**, *1*, 3–15. [CrossRef]
12. De La Torre, D.; Ortega, A. Variability and Wave Power for Open Ocean Wave Conditions of the Peru Basin. In Proceedings of the 2022 IEEE Engineering International Research Conference, Lima, Peru, 26–28 October 2022. [CrossRef]
13. De La Torre, D.; Ortega, A. Applicability of the Standard Sea Spectrums and New Calibration Coefficients for the Wave Energy Period Calculation of the Peru Sea Basin. In Proceedings of the 2022 IEEE Engineering International Research Conference, Lima, Peru, 26–28 October 2022. [CrossRef]
14. Gommenginger, C.P.; Srokosz, M.A.; Challenor, P.G. Measuring ocean wave period with satellite altimeters: A simple empirical model. *Geophys. Res. Lett.* **2003**, *30*, 22. [CrossRef]
15. Badulin, S.I. A physical model of sea wave period from altimeter data. *J. Geophys. Res. Oceans* **2014**, *119*, 856–869. [CrossRef]
16. Badulin, S.I.; Zakharov, V.E. The Phillips spectrum and a model of wind-wave dissipation. *Theor. Math. Phys.* **2020**, *202*, 309–318. [CrossRef]
17. Phillips, O.M. The equilibrium range in the spectrum of wind-generated waves. *J. Fluid Mech.* **1958**, *4*, 426–434. [CrossRef]
18. Ahn, S.; Neary, V.S.; Ha, T. A practical method for modeling temporal-averaged ocean wave frequency-directional spectra for characterizing wave energy climates. *Renew. Energy* **2023**, *207*, 499–511. [CrossRef]
19. Kardakaris, K.; Dimitriadis, P.; Iliopoulou, T.; Koutsoyiannis, D. Stochastic simulation of wind wave parameters for energy production. *Ocean Eng.* **2023**, *274*, 114029. [CrossRef]
20. Andrews, D.G.; McIntyre, M.E. On wave-action and its relatives. *J. Fluid Mech.* **1978**, *89*, 647–664. [CrossRef]
21. Roland, A.; Ardhuin, F. On the developments of spectral wave models: Numerics and parameterizations for the coastal ocean. *Ocean Dyn.* **2014**, *64*, 833–846. [CrossRef]
22. WAVEWATCH-III. v6.07.1. Available online: <https://github.com/NOAA-EMC/WW3/releases/tag/6.07.1> (accessed on 30 April 2023).
23. Liu, Q.; Rogers, W.E.; Babanin, A.V.; Young, I.R.; Romero, L.; Zieger, S.; Qiao, F.; Guan, C. Observation-Based Source Terms in the Third-Generation Wave Model WAVEWATCH III: Updates and Verification. *J. Phys. Oceanogr.* **2019**, *49*, 489–517. [CrossRef]
24. Amarouche, K.; Akpınar, A.; Rybalko, A.; Myslenkov, S. Assessment of SWAN and WAVEWATCH-III models regarding the directional wave spectra estimates based on Eastern Black Sea measurements. *Ocean Eng.* **2023**, *272*, 113944. [CrossRef]
25. SWAN—Simulating Waves Nearshore. Available online: <https://swanmodel.sourceforge.io> (accessed on 2 May 2023).
26. National Data Buoy Center. Available online: <https://www.ndbc.noaa.gov/> (accessed on 7 January 2023).
27. De La Torre, D.; Ortega, A. Wave Energy Distribution and Directional Assessment in the Peru Basin. In Proceedings of the 2022 IEEE XXIX International Conference on Electronics, Electrical Engineering and Computing, Lima, Peru, 11–13 August 2022. [CrossRef]
28. Holthuijsen, L.H. Statistics. In *Waves in Ocean and Coastal Waters*; Cambridge University Press: New York, NY, USA, 2007.
29. Folley, M. The Wave Energy Resource. In *Handbook of Ocean Wave Energy*; Pecher, A., Kofoed, J.P., Eds.; Springer: Cham, Switzerland, 2017; Volume 7. [CrossRef]
30. Beck, R.F.; Cummins, W.E.; Dalzell, J.F.; Mandel, P.; Webster, W.C. Motions in Waves. In *Principles of Naval Architecture*, 3rd ed.; Lewis, E.V., Ed.; The Society of Naval Architects and Marine Engineers: Jersey City, NJ, USA, 1989; Volume III.
31. Sierra, J.P.; White, A.; Mosso, C.; Mestres, M. Assessment of the intra-annual and inter-annual variability of the wave energy resource in the Bay of Biscay (France). *Energy* **2017**, *141*, 853–868. [CrossRef]
32. Hagerman, G. Southern New England Wave Energy Resource Potential. In Proceedings of the Building Energy, Boston, MA, USA, 21–24 March 2001.
33. Contestabile, P.; Russo, S.; Azzellino, A.; Cascetta, F.; Vicinanza, D. Combination of local sea winds/land breezes and nearshore wave energy resource: Case study at MaRELab (Naples, Italy). *Energy Convers. Manag.* **2022**, *257*, 115356. [CrossRef]
34. Guillou, N.; Lavidas, G.; Chapalain, G. Wave Energy Resource Assessment for Exploitation—A Review. *J. Mar. Sci. Eng.* **2020**, *8*, 705. [CrossRef]
35. ABP mer. *Atlas of UK Marine Renewable Resources*; Technical Report; ABP Marine Environmental Research Ltd.: Southampton, UK, 2008.
36. Contestabile, P.; Ferrante, V.; Vicinanza, D. Wave Energy Resource along the Coast of Santa Catarina (Brazil). *Energies* **2015**, *8*, 14219–14243. [CrossRef]
37. Contestabile, P.; Lauro, E.D.; Galli, P.; Corselli, C.; Vicinanza, D. Offshore Wind and Wave Energy Assessment around Malè and Magoodhoo Island (Maldives). *Sustainability* **2017**, *9*, 613. [CrossRef]

38. Hastie, T.; Tibshirani, R.; Friedman, J. Kernel Smoothing Methods. In *The Elements of Statistical Learning*; Springer: New York, NY, USA, 2009. [[CrossRef](#)]
39. El Niño & La Niña. Available online: <https://www.climate.gov/enso> (accessed on 7 February 2023).

Disclaimer/Publisher's Note: The statements, opinions and data contained in all publications are solely those of the individual author(s) and contributor(s) and not of MDPI and/or the editor(s). MDPI and/or the editor(s) disclaim responsibility for any injury to people or property resulting from any ideas, methods, instructions or products referred to in the content.